ACS APPLIED ELECTRONIC MATERIALS

pubs.acs.org/acsaelm Article

Charge Transport through Superexchange in Phenothiazine−7,7,8,8-Tetracyanoquinodimethane (PTZ−TCNQ) Cocrystal Microribbon FETs Grown Using Evaporative Alignment

Scott Melis, Samantha Hung, Chaitali Bagade, Yuri Chung, Eleni Hughes, Xinran Zhang, Paola Barbara, Peize Han, Tingting Li, Daniel McCusker, Robert Hartsmith, Jeffery Bertke, Pratibha Dev, Iris Stone, Jaydeep Joshi, Patrick Vora, and Edward Van Keuren*

Cite This: https://doi.org/10.1021/acsaelm.2c01160 Read Online

ACCESS | Metrics & More | Article Recommendations | Supporting Information

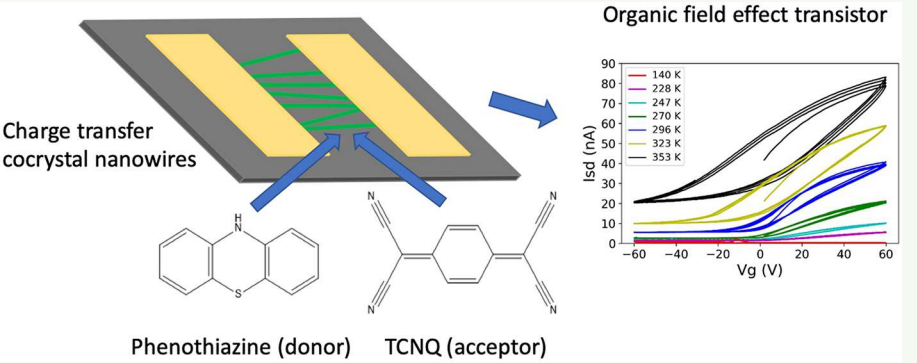

ABSTRACT: Charge transfer (CT) cocrystals, molecular crystals composed of electron donating and accepting species, are being developed for applications in optoelectronics. Here we present optical and electronic characterization of the CT cocrystal phenothiazine−tetracyanoquinodimethane (PTZ−TCNQ). This material has a broad NIR absorption peak with an optical band edge less than 0.6 eV. We used density functional theory calculations to identify the origin of the low energy CT states and changes in the Raman spectra. We also demonstrate the fabrication of long, ribbon-like oriented cocrystals using an evaporative alignment method. Cocrystals grown on Si substrates were fabricated into organic field effect transistors. Despite theoretical predictions of ambipolarity, only electron conduction was observed, with mobilities on the order of 10^{-4} cm^2 V^{-1} s^{-1}. Measurements of the temperature dependence of the mobility indicated a superexchange mediated hopping mechanism for charge transport, with a characteristic energy scale of 0.19 eV.

KEYWORDS: *charge-transfer crystal, organic field effect transistor, evaporative self-assembly, directed growth, superexchange charge transport*

INTRODUCTION

Organic semiconductors have been extensively investigated over the past several decades for the development of inexpensive, flexible, and potentially disposable electronics that would complement those fabricated from inorganic materials. Unipolar organic field effect transistors (OFETs) date back to the late 1980s,[1] and significant research effort since that time has focused on developing new organic semiconducting materials.[2,3] More recently, there has been considerable interest in utilizing the ambipolar charge transport that some organic materials display to create novel types of devices.[3,4]

Charge transfer (CT) cocrystals are molecular crystals composed of electron donor and acceptor molecules in either segregated or mixed stack arrangements.[5−7] Most mixed stack cocrystals are semiconductors and, depending on the constituent molecules, can display very different behaviors, including ferroelectricity,[8] superconductivity,[9] and large photoconductivity.[10] Many of them can be grown in nanowire forms which can be aligned and therefore easily integrated into devices.[11]

Both ground and exited states of CT cocrystals have some degree of electron transfer from donor to acceptor. The

Received: August 31, 2022
Accepted: November 9, 2022

associated changes in the wave functions typically result in a new peak in the optical absorption spectrum, usually at a lower energy than the HOMO−LUMO transitions of the individual donor and acceptor molecules.[12] In addition, large charge carrier mobilities have been measured in some systems; for example, Takahashi et al. found electron mobilities ∼1 $cm^2 V^{-1} s^{-1}$ in DBTTF−TCNQ (dibenzotetrathiafulvalene−7,7,8,8-tetracyanoquinodimethane).[13] Recent reports have also suggested that particular combinations of donor and acceptor molecules can lead to CT crystals that have balanced electron and hole mobilities as large as 0.05 $cm^2 V^{-1} s^{-1}$, making them promising as materials for ambipolar OFET applications.[14,15]

Zhu et al. performed a systematic computational study of a number of charge transfer crystals and reported calculations of the effective masses for electrons and holes.[14] Of the materials they investigated, the mixed-stack CT crystal composed of the electron donor phenothiazine (PTZ) and the electron acceptor 7,7,8,8-tetracyanoquinodimethane (TCNQ), shown in Figure 1, showed low values for the effective masses for both carriers

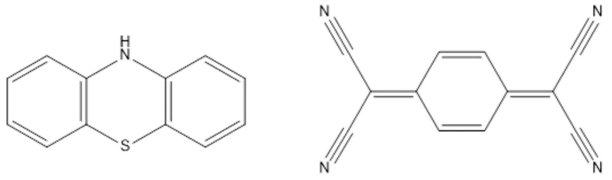

Figure 1. Molecular structures of phenothiazine (left) and TCNQ (right).

that were on the same order of magnitude: $m_e = 0.51m_0$ and $m_h = 0.50m_0$ for the $C2/c$-symmetry cocrystal. These imply balanced charge transport with good charge carrier mobility. They also calculated a low band gap of around 0.5 eV in this material that is consistent with experimental measurements of bulk cocrystals.

PTZ is a compound used in a number of medical applications, for example, as an antibacterial and antifungal agent.[16] TCNQ is one of the strongest organic electron acceptors known and has been used in numerous charge transfer complexes with donors such as tetrathiafulvalene[17] and perylene.[18] These two compounds have been shown to form a mixed-stack charge transfer complex in bulk form,[19,20] and recently microwire FETs of this cocrystal have been reported.[21]

To be useful for optical and electronic applications, cocrystals must be able to be formed using simple, scalable methods. Controlled alignment of the crystal axis is also important because most of these materials have anisotropic electronic and optical properties. There has been a considerable amount of recent research on the formation and alignment of nanowires of organic crystals over the past several decades.[11,22] Various methods have been developed for controlling the growth to be preferentially along the stacking direction and aligned along a particular direction, including dewetting induced crystallization,[23] dip coating,[24] and the Marangoni effect.[25] The controlled evaporative self-assembly (CESA) method developed by Han and Lin,[26] and applied to OFETS by Bi et al.,[27] has been shown to be an effective method for obtaining well-aligned nano- and microwires of organic crystals. In this method, the crystal aligns through solvent evaporation in the presence of capillary forces. These forces arise from the meniscus of the solvent created by a glass cylinder placed on top of the drying solution. A schematic of the method is shown in Figure 2.

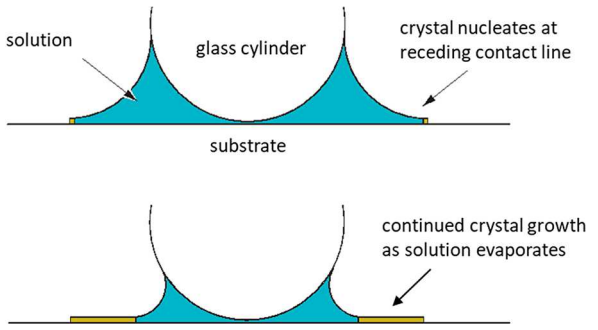

Figure 2. Diagram of the CESA method.

Here we demonstrate the formation of ordered cocrystals of PTZ−TCNQ using the CESA method. This fabrication method has a substantial advantage of being easily adaptable to roll-to-roll processing of printed electronics, and to our knowledge, this is the first use of it to create devices from CT cocrystals. The cocrystals formed long microribbons, from which we fabricated field effect transistors and measured the mobility as a function of temperature. Contrary to theoretical predictions, we observed primarily electron transport, with a modest value for mobility. The temperature-dependent mobility suggests hopping through a superexchange coupling as the primary mechanism of charge transport.[28]

EXPERIMENTAL METHODS

Aligned cocrystals for devices were prepared using the controlled evaporative self-assembly (CESA) method directly from acetone solutions. Both components were dissolved in acetone at equal concentrations of 1 mmol. An 8 mm diameter glass cylinder was placed onto the substrate, and 0.02 mL of solution was pipetted onto the cylinder. The solution gathered at the interface between cylinder and substrate, where it wicked along the gap between the glass rod and the substrate. The solvent was allowed to dry over 6 min, resulting in only cocrystals remaining on the substrate.

Samples for characterization via UV−vis−NIR spectroscopy and optical microscopy were grown using glass microscope slides as the substrate. The slides were rinsed with acetone prior to deposition. Similarly, samples for X-ray diffraction were grown on a glass microscope coverslip.

For Raman spectroscopy and OFET fabrication, the crystals were deposited on P-doped Si wafers with a 285 nm oxide layer grown on them. To make the OFETs, a CVC magnetron sputtering system was used with a metal shadow mask (see Figure S1) to deposit electrodes consisting of a 15 nm thick adhesion layer of Titanium followed by a 500 nm layer of gold. The channel length was 85 μm and the width was 3 mm, although the entire channels were generally not completely covered with the crystals. Optical microscopy images of the devices were used to determine the effective channel lengths by measuring the area of the gap that was covered by the crystals.

Absorption spectra were taken with a Cary 5000 UV−vis−NIR spectrophotometer in transmission mode. Optical images were taken on a Zeiss upright microscope using a 20× objective. Powder X-ray diffraction patterns were collected on a zero-background Si wafer sample holder using a Rigaku Ultima IV X-ray powder diffractometer with Cu Kα radiation at 40 kV and 30 mA and a D/teX silicon strip detector. SEM images were taken with a Zeiss Supra 55VP with an in-lens detector at 5 kV beam energy. Silicon wafers with samples were diced and imaged directly.

Atomic force microscopy (AFM) and Kelvin probe force microscopy (KPFM) were performed on cocrystal samples using a

https://doi.org/10.1021/acsaelm.2c01160
ACS Appl. Electron. Mater. XXXX, XXX, XXX−XXX

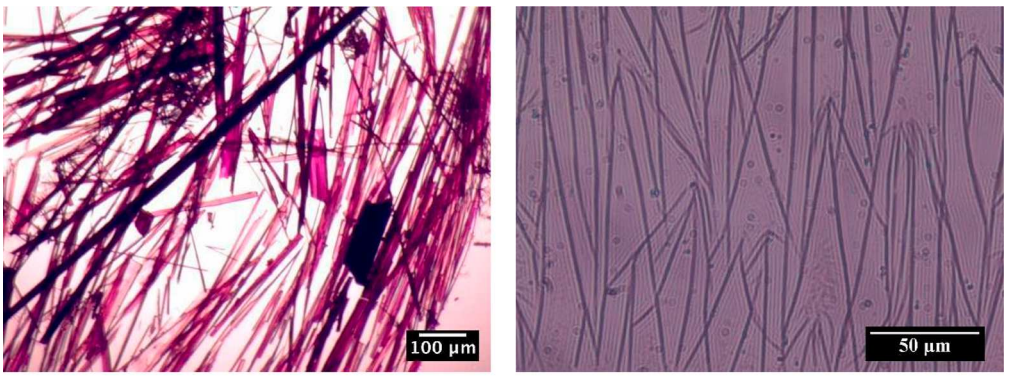

Figure 3. Optical images of bulk PTZ−TCNQ cocrystals grown from solution (a) and grown using CESA (b).

NTEGA Prima AFM. For AFM, a silicon probe (cantilever force constant ∼3.5 N/m) was operated in tapping mode, with a scanning rate of 0.5 Hz. For two-pass KPFM, the sample surface was connected to the ground via a metal clip, and a silicon probe with gold or titanium nitride-coated tip (cantilever force constant ∼10 N/m) was used. A slower scanning rate (0.2 Hz) was needed due to the relatively large variation in surface height.

Electronic characterization was done using a probe station consisting of three micromanipulators connected to an HP 4140B pA meter/voltage source. The instrument was controlled by a LabView program that swept the applied voltage and measured the corresponding current. Temperature-dependent measurements of the transfer curves in the range from 280 to 350 K were done using a Peltier heater that was controlled by a TC-720 thermoelectric temperature controller. A silicon wafer containing the test devices was attached to the Peltier heater using thermal grease. A feedback thermistor to monitor the temperature of the wafer was also attached using thermal grease ∼5 mm away from the device being tested.

For temperatures from 120 to 293 K, devices were measured in a cryostat at a vacuum pressure of $\sim 5 \times 10^{-5}$ Torr. Using conductive silver paste, leads were attached to the existing gold electrodes to interface with the cryostat system. No significant difference in device performance was observed at room temperature between the two temperature-controlled setups, indicating that the vacuum pressure and extension wires did not significantly alter device performance.

RESULTS AND DISCUSSION

Synthesis of Oriented Cocrystals. PTZ−TCNQ showed a preference for crystallizing in needle-like morphology, as shown in bulk cocrystals prepared by solvent evaporation. Using the CESA method, we were able to grow oriented ribbon-like cocrystals as shown in an optical microscopy image in Figure 3. We found that the solvent can play an important role in the formation and orientation of crystals formed using CESA[29] and that acetone works well to produce long, well-aligned crystals.

AFM measurements, an example of which is shown in Figure 4, indicated that the cocrystal morphology was that of ribbons, with thicknesses of the order of 100 nm and width 1−2 μm. This is similar to other materials we have grown using CESA, including perylene−TCNQ[30] and polydiacetylene.[29]

Cocrystals prepared using CESA were too thin and narrow for single crystal X-ray diffraction measurements, but powder X-ray diffraction data are shown in Figure 5, along with the known peaks for bulk PTZ−TCNQ from the Cambridge Structural Database.[31−33] The spectrum matches the two main peaks for the cocrystal ([021] and [040] planes). Because the X-ray diffraction is at a fixed orientation with respect to the

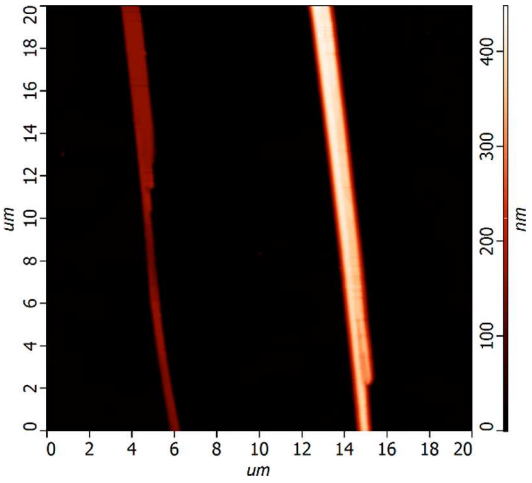

Figure 4. AFM images of PTZ−TCNQ cocrystals.

crystal axis, it might not display all peaks as in a powder X-ray spectrum. In addition, we see a large peak that appears to be from pure phenothiazine and possibly some contribution of TCNQ as well. This may be from regions of the film at the start or end of the CESA crystal formation as the area probed spans the entire growth length of the substrate. We have shown that in cocrystal formation by evaporation the stoichiometry that forms is influenced by both the phase diagram and the initial solution concentration, and pure crystals may form at the beginning or end of the process.[30]

Spectra taken with different orientations of the ribbons with respect to the scattering plane showed the same peaks but different relative ratios. In particular, the peak at 13.8° corresponding to the [040] plane showed a pronounced increase relative to the peaks at other angles for ribbons oriented perpendicular to the scattering plane (see Figure S2). This suggests that the long axis of the ribbons coincides with the stacking direction of the cocrystals. This alignment is observed in other cocrystals fabricated using CESA,[30] as well as similar to the needle-like crystals that typically form for bulk PTZ−TCNQ.[31−33] It was also corroborated by the charge carrier mobility values presented later, which are predicted to be substantial only along the crystal stacking axis.

Raman spectroscopy provided further evidence for the cocrystal formation by demonstrating a shift in the peaks of the TCNQ molecule. Figure 6 shows the Raman spectra of a ribbon of PTZ−TCNQ prepared using CESA and pure

https://doi.org/10.1021/acsaelm.2c01160
ACS Appl. Electron. Mater. XXXX, XXX, XXX−XXX

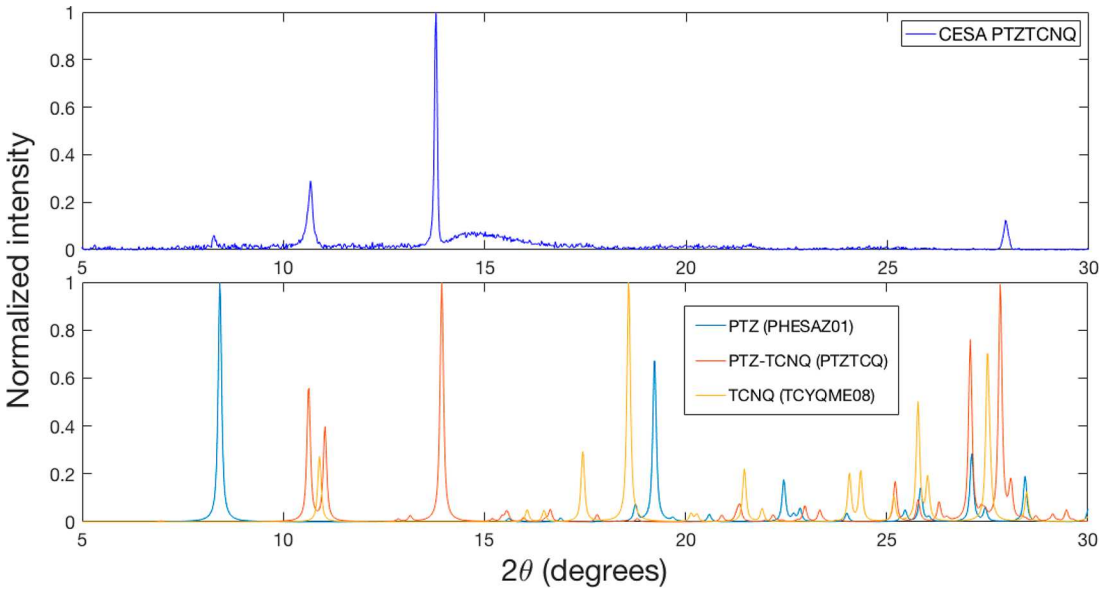

Figure 5. X-ray diffraction spectra of the PTZ−TCNQ cocrystals grown using CESA (top), shown along with spectra of bulk PTZ−TCNQ (PTZTCQ), pure PTZ (PHESAZ01), and pure TCNQ (TCYQME08) from the CSD (the abbreviations are those used in the database).

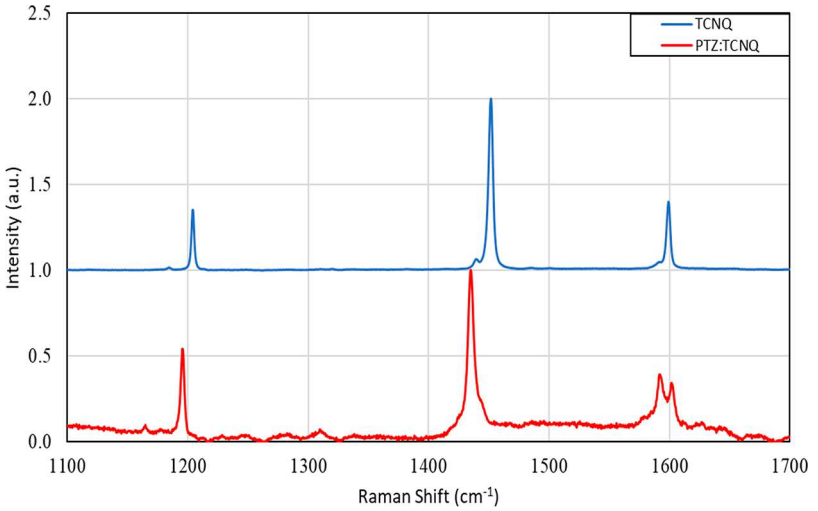

Figure 6. Raman spectra of PTZ−TCNQ and pure crystals of TCNQ. Crystals of pure PTZ had too strong of a fluorescence signal to obtain a clear Raman spectrum.

TCNQ nanocrystals. Most of the prominent peaks in this region are from TCNQ: a peak at 1207 cm^{-1} attributed to a CH bend and peaks at 1454 and 1602 cm^{-1} associated with C═C stretch modes.[34] We were unable to obtain a clear Raman spectrum of PTZ due to the large background fluorescence, but its spectrum has been reported in the literature as having a strong peak at 1040 cm^{-1}, attributed to a CH ring deformation, along with moderate peaks at 1250 (symmetric Ph−N−Ph stretch mode), 1570, and 1605 cm^{-1} (ring stretch modes).[35] Interestingly, in the cocrystal we only observed the PTZ peak at 1605 cm^{-1}. The other PTZ modes may be quenched in the cocrystal or simply much weaker than those from TCNQ.

The red-shift in the TCNQ C═C stretch peak at 1454 cm^{-1} in the cocrystal has been attributed to the changes due to the charge transfer.[36] The peaks in the cocrystal made with CESA matched well with those of PTZ−TCNQ cocrystals grown by the reprecipitation method, a method of forming crystals by rapidly mixing with a poor solvent.[37] Temperature-dependent Raman spectroscopy was also performed, and results are shown in Figures S3−S5.

Figure 7 shows UV−vis−NIR optical absorption spectra of pure PTZ, pure TCNQ, and the cocrystal prepared using CESA. Compared to crystals of the individual coformers, which have absorption maxima in the blue/UV range, the cocrystal displays a broad IR absorption band centered at roughly 1500 nm (0.83 eV), in agreement with measured[21,38] and calculated[14] values of the bulk cocrystals.

Molecular Modeling. Density functional theory (DFT) calculations were performed using the Gaussian09[39] software suite. The hybrid functional, B3LYP (Becke-3 Lee−Yang−Parr),[40−42] was used to approximate the exchange−correlation (xc) energy functional. B3LYP adds a fixed percentage (20%) of exact exchange to the xc-functional, improving upon the more traditional approximations to the xc-functional. We performed all calculations with two different basis sets: (i) the

https://doi.org/10.1021/acsaelm.2c01160
ACS Appl. Electron. Mater. XXXX, XXX, XXX−XXX

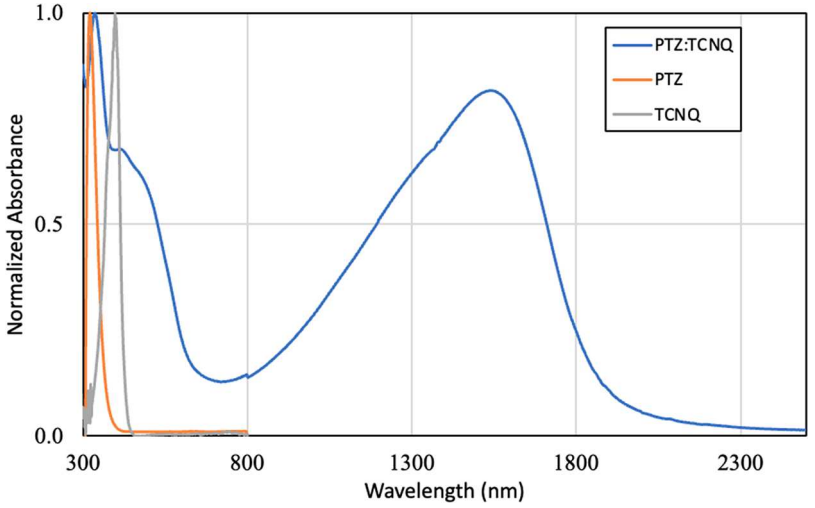

Figure 7. Absorption spectrum of 1:1 PTZ−TCNQ cocrystals along with pure crystals of PTZ and TCNQ. The large, broad peak centered at 1540 nm corresponds to the absorption by the CT band.

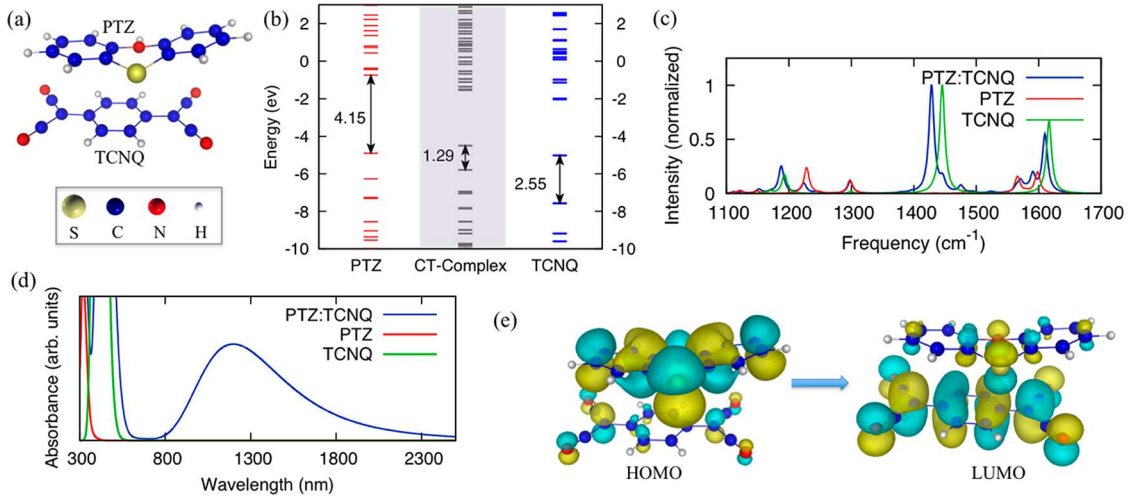

Figure 8. Molecular modeling. (a) Equilibrium structure of the PTZ−TCNQ composite (b) Single-particle energy levels (c) Scaled Raman spectra (scaling factor = 0.97) of individual molecules and their composite, showing the origin of additional lines around ∼1602 cm^{-1} line to be due to Raman-active modes that are mostly localized on PTZ. (d) Theoretical UV−vis spectra of individual molecules and their composite. (e) Lowest energy transition in the UV−vis spectrum of the composite corresponds to the charge-transfer transition from the HOMO (mostly localized on electron donor PTZ) to the LUMO (mostly localized on TCNQ).

standard 6-31G* and (ii) the larger 6-311G** basis set. We find a very good agreement for the singlet excitation energies obtained from our time-dependent DFT (TD-DFT) calculations using the two basis sets, as was also reported in earlier studies of organic molecules.[43] On the other hand, in the case of the Raman spectra, we find a much better agreement between experiment and theory when the larger 6-311G** basis set is employed. Hence, we report our results obtained with this larger basis set.

We calculated the ground- and excited-state properties of the individual molecules and compared those with the properties of a simpler PTZ−TCNQ complex containing a single molecule of each species. Although this complex is not an infinite structure representing the bulk material, it captures the most salient features of the Raman and UV−vis spectra of the cocrystals and can be used as a model structure to illustrate the changes in properties when the individual constituent molecules are brought together to form the cocrystals. Figure 8a shows the optimized structure for the PTZ−TCNQ complex. Figure 8b is an energy-level diagram showing alignment of levels corresponding to the molecular orbitals of the isolated PTZ molecule (in red), TCNQ molecule (in blue), and the PTZ−TCNQ charge-transfer complex (in gray) within the B3LYP approximation. The gaps between the highest and the lowest occupied molecular orbitals (HOMO−LUMO gaps) are also given in the figure. We find that the CT complex has a much smaller HOMO−LUMO difference than either of the constituent molecules. Furthermore, our calculations show that a net charge of ∼0.18e is transferred from the electron donor, PTZ, to the electron acceptor, TCNQ.

We further used DFT to calculate the Raman spectra of the PTZ−TCNQ complex along with those of the isolated molecules. DFT is known to overestimate the calculated values of Raman frequencies relative to the experimental results.[44] Hence, the theoretical Raman spectra for the three structures in Figure 8c are scaled uniformly, allowing comparison with experiment. A scaling factor of 0.97 gives a

https://doi.org/10.1021/acsaelm.2c01160
ACS Appl. Electron. Mater. XXXX, XXX, XXX−XXX

good agreement (to within ±15 cm^{-1}) between the theoretical results and the measured Raman spectra (cf. Figure 6). The scaling factor employed here is consistent with the commonly used values in the theoretical studies of Raman spectra.[45] We also identify the source of the observed (apparent) splitting of the 1602 cm^{-1} line, which is associated with the TCNQ's C═C stretch mode. This apparent splitting is found to instead be due to vibrational modes that are mostly localized on the PTZ molecule within the complex.

To further understand the properties of the cocrystals, we also calculated the UV−vis spectra of the PTZ−TCNQ complex and the individual, isolated molecules using TD-DFT. The UV−vis spectrum of our model complex is found to be in qualitative agreement with the experimental spectrum for the cocrystal, with the smallest energy excitation of the PTZ−TCNQ complex (Figure 8d) occurring at 1198.20 nm (1.03 eV). It is larger than the measured absorption maximum shown in Figure 7; however, this may simply be due to the fact that the calculation was done for a dimer, while the measured spectra were from cocrystals. Long-range ordering in a CT cocrystal can lead to decreases in the HOMO−LUMO energy difference compared to that in the dimer complex and may also affect the degree of charge transfer, which was measured to be 0.31 (see the following section). Figure 8e shows the isosurface plots for the frontier orbitals involved in the lowest energy transition in the UV−vis spectrum of the composite, corresponding to the charge-transfer transition from the HOMO (mostly localized on electron donor PTZ) to the LUMO (mostly localized on TCNQ). Hence, this transition will lead to sufficient charge separation, ensuring reduced charge recombination upon excitation. The next excitation with a large oscillator strength (460.51 nm/2.69 eV) involves transitions from deeper states (HOMO−1, HOMO−2, HOMO−3, and HOMO−4) to the LUMO. This transition has a mixed local and charge transfer character, with the HOMO−3 and HOMO−4 mostly localized on the PTZ molecule within the complex, while the other two orbitals have considerable contributions from the molecular orbitals of TCNQ. The mixed character of the excitations (charge transfer and local) may play a role in the efficiency of the cocrystal in optoelectronic applications.

Degree of Charge Transfer. The charge transfer interaction in a mixed-stack structure can be modeled by assuming the overlap (transfer integral) between adjacent molecules is small compared to other energies in the system so that the electrons are highly localized onto their corresponding molecules. The energy involved in the transfer of charge is that of ionizing a donor−acceptor pair and the electrostatic Madelung energy gained if the molecular lattice is ionic.[46] The cost of ionizing the donor−acceptor pair is given by the difference between the ionization potential of the donor, I, and the electron affinity of the acceptor, A. The Madelung energy is given by $\alpha\langle e^2/a\rangle$, where α is the Madelung constant and the term in parentheses represents the averaged electrostatic interaction between a neighboring donor and acceptor molecule separated by distance a. The total energy per donor−acceptor pair is given by

$$E(\rho) = (I - A)\rho - \alpha\left\langle \frac{e^2}{a} \right\rangle \rho^2 \quad (1)$$

where ρ is the degree of charge transfer between the donor and acceptor molecules ($0 \leq \rho \leq 1$, where a value of 0 reflects a neutral solid while a ρ value of 1 indicates a completely ionic compound). Most charge transfer crystals will have intermediate values of ρ, indicating partial charge transfer.

The value of the ground-state charge transfer, ρ, can be estimated using Raman spectroscopy, as demonstrated by Matsuzaki et al. in their work on TCNQ salts.[36] They showed that shifts in the C═C stretch mode of the TCNQ at wavenumber 1454 cm^{-1} corresponded to the degree of charge transfer. From the 19 cm^{-1} shift of this peak shown in Figure 6, we find a value ρ = 0.31 for PTZ−TCNQ, indicating a moderate amount of charge transfer. This value is somewhat larger than that determined by Tanaka et al. using the measured oscillator strength of the CT transition in a bulk crystal.[20]

Torrance et al. showed that CT cocrystals can be classified as either ionic or neutral depending on $I - A$, with a phase transition occurring near the Madelung energy $\alpha\langle e^2/a\rangle$.[46] Using the value for $\alpha\langle e^2/a\rangle \sim 4.1$ eV found by Torrance et al., I = 7.02 eV reported by Bloor et al. for phenothiazine,[47] and A = 3.38 eV for TCNQ measured by Zhu and Wang,[48] we find that PTZ−TCNQ is close to the transition, but slightly on the ionic side, matching the results of the charge transfer value determined from the Raman spectra. The dependence of the frequency of the optical absorption of the CT transition, ν_{CT}, on $I - A$ was determined by Torrance to be

$$h\nu_{CT} = (I - A) - \langle e^2/a\rangle \quad (2)$$

This gives an optical absorption energy transition of 1.13 eV, comparable to the measured value of 0.83 eV.

We also investigated the temperature dependence of the Raman spectra. We saw clear red-shifts of lines associated with some of the peaks, for example, the TCNQ C═C stretching mode at 1640 cm^{-1}, but no changes in the TCNQ 1454 cm^{-1} peak that is sensitive to the degree of charge transfer, suggesting that there is negligible temperature dependence of ρ (see Figures S4 and S5).

Charge Transport. As mentioned earlier, there have been several reports of ambipolarity in PTZ−TCNQ, both computational and experimental. However, charge transport in organic devices may be influenced by properties other than the intrinsic mobility, including trap states, charge injection at the electrodes, and material doping.[49] To measure the charge carrier mobility in PTZ−TCNQ, we fabricated OFETs using the CESA method to create an array of ribbons to serve as the active layer. Some of the ribbons contain bends, which are likely to reduce mobility, or splits, which may affect transport if branches do not reach the electrodes. Ribbons also overlap, which could also affect mobility due to the mechanical stress on the cocrystals.

Initial devices were fabricated using a bottom electrode configuration, in which the cocrystals were deposited on gold source and drain electrodes that had been previously deposited on a Si/SiO_2 wafer. While this produced functioning devices, they suffered from low mobilities and large amounts of hysteresis. To improve the performance, we fabricated top electrode devices, a schematic of which is shown in Figure 9. PTZ−TCNQ cocrystals were grown directly onto a 4 in. Si/SiO_2 wafer using the CESA method as described earlier. Gold electrodes with a titanium adhesion layer were then sputtered directly on top of the semiconducting cocrystals through a shadow mask, producing a more effective direct contact between the metal and the cocrystal channel. The deposition rate of the gold layer needed to be slow (0.8 Å/s) to prevent

https://doi.org/10.1021/acsaelm.2c01160
ACS Appl. Electron. Mater. XXXX, XXX, XXX−XXX

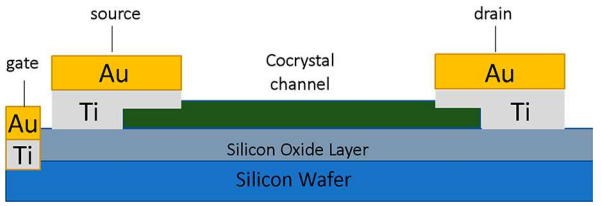

Figure 9. Top contact bottom gate device configuration (not to scale). PTZ−TCNQ is grown using the CESA method directly onto the oxide layer of a silicon wafer. The oxide under the gate electrode was scratched away to obtain an electrical contact to the doped Si substrate. The electrodes were patterned by using a shadow mask.

damage to the crystals under the metal mask, an effect that we observed at higher deposition rates. This was most likely due to heating of the metal shadow mask caused by the prolonged bombardment of Au ions. More details concerning the shadow masks and deposition conditions are given in the Supporting Information (Figure S1). An SEM image of the cocrystals in a functional device is shown in Figure 10.

Device performance using these electrodes was consistent across multiple (15) samples. An example transfer curve, in which the source drain voltage is fixed and the current measured as the gate voltage is swept, is shown in Figure 11. The inset shows the current as a function of source−drain voltage with no gate voltage applied.

As described in several previous works (see for example ref 13), the sign of the charge carriers is mainly determined by the alignment of the electrode work function with respect to the semiconductor HOMO−LUMO gap. Good alignment of the electrode work function with the LUMO (HOMO) is necessary to yield good ohmic contact for the injection of electrons (holes). Alignment of the electrode work function in the middle of the gap can yield ambipolar transport for materials with a narrow bandgap and sufficiently low injection barrier. Ambipolar transport for an individual PTZ−TCNQ cocrystal was indeed reported by Li et al. with a source−drain voltage as high as 40 V and gate voltage varying from −40 to +40 V.[21] The output curves were not reported. The transfer characteristics of our devices only show an increase in current in the positive gate voltage range, as shown in Figure 11, while

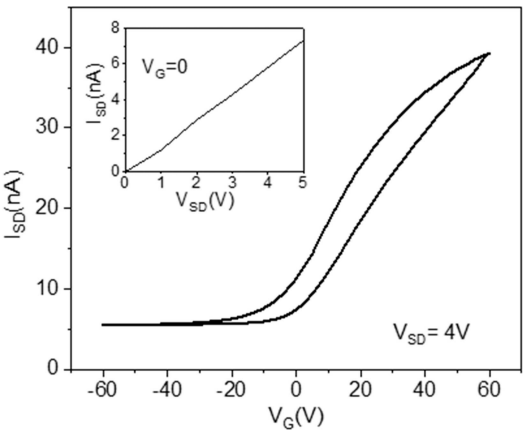

Figure 11. Example of a typical transfer curve at room temperature and in ambient conditions for top contact bottom gate PTZ−TCNQ FETs. The inset shows the linear output curve at zero gate voltage.

the linear dependence of the output curves indicate ohmic contacts or small Schottky barriers for the charge carriers. These results suggest that the electrode work function is aligned closer to the LUMO energy, yielding n-type transport. To confirm this, we performed Kelvin probe measurements of the cocrystals on a Au surface. As shown from the surface potential change plotted in Figure S6, the Au work function is smaller than the work function of the cocrystal by a few hundred millielectronvolts. Assuming that the doping of our PTZ−TCNQ cocrystals is low and that we can approximate its electrochemical potential in a midgap position (see, e.g., ref 50), our Kelvin probe measurements indicate that the Au electrode work function is aligned closer to the LUMO, consistent with electron transport. However, because the transfer characteristic shows a considerable amount of hysteresis, specifically, lower back sweep current (BSC) hysteresis, we cannot exclude the possibility that hole traps may contribute to the lack of hole transport in the devices. Hysteresis caused by trap states is common in organic semiconductors.[51] Attempts to reduce these traps using surface modification of the substrate were so far unsuccessful because these changes significantly affected the cocrystal deposition.

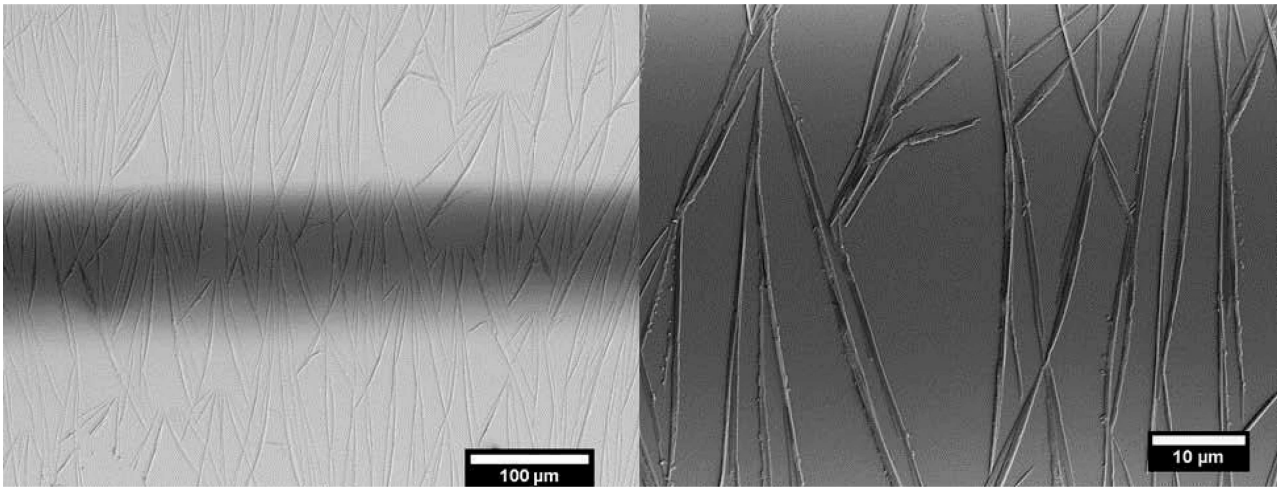

Figure 10. SEM images of PTZ−TCNQ cocrystals in the top contact bottom gate electrode configuration. The left image shows the metal electrodes (in the brighter areas) and the exposed cocrystals in the gap. The right image is a magnified image of the center of the left image showing the cocrystals.

https://doi.org/10.1021/acsaelm.2c01160
ACS Appl. Electron. Mater. XXXX, XXX, XXX−XXX

Future work will focus on the study of these trap states to possibly reduce the hysteresis and improve the device quality. In particular, the effect on the electronic properties of the branching and/or twinning of the cocrystals, observed in Figure 10, as well as other possible crystal defects, requires further investigations.

For both p- and n-type transfer curves, if V_{SD} is small relative to V_G, there is a region for low V_G (close to 0 V) in which the device's response can be approximated to be linear. In this case, the charge carrier mobility for either holes or electrons, μ, can be determined using

$$I_{SD} = \mu C_A \frac{W}{L}\left(V_G V_{SD} - \frac{{V_{SD}}^2}{2}\right) \quad (3)$$

$$\mu = \frac{dI_{SD}}{dV_G}\frac{L}{C_A W V_{SD}} \quad (4)$$

where I_{SD} is the source−drain current, V_{SD} is the source−drain voltage, V_G is the gate voltage, C_A is the capacitance per unit area between the semiconducting material and the gate electrode, and L and W are the length and width of the semiconducting channel.[52] For small V_{SD} values, eq 4 can be derived from eq 3, and a value for the mobility can be determined using a linear fit to the I_{SD} vs V_G data. A mobility of 3×10^{-4} cm^2/(V s) was determined from the data shown in Figure 11. The linear fit for the mobility was performed on the forward (upper) path of the hysteresis loop in the region of the gate voltage between 5 and 20 V. The channel width was approximated as the total area covered by the cocrystals divided by the channel length, in other words, the widths of the fibers times the number of fibers in the device.

Temperature-Dependent Mobility and Conduction Mechanism. In organic molecular crystals the mobility μ is often categorized using either a band conduction model for high mobility conductors ($\mu \gg 1$ cm^2/(V s)) in which the mobility scales with temperature as T^{-n} or a hopping model for low mobility conductors ($\mu \ll 1$ cm^2/(V s)) which scales as $\exp(-E_A/k_B T)$, where E_A is the activation energy.[53] Hopping and variable range hopping developed as concepts to explain the conduction mechanism in materials in which charge carriers are in localized energy states and a traditional conduction band does not exist.[54] Although this analysis was originally proposed for amorphous organic transistors, it has been applied to a variety of systems, including organic molecular crystals.[55]

In CT cocrystals, hopping of electrons (holes) would occur between two donors (acceptors), and therefore need to occur across the intermediate acceptor (donor) molecule. Geng et al. developed a superexchange model to describe the charge transport in several CT cocrystals.[28,56] They showed that the acceptor acts as a bridge for the electron to hop between donor sites and the donor acts as a bridge for the hole to hop between acceptor sites. In PTZ−TCNQ, one of the cocrystals they studied, they also found similar values for the electron and holes masses, implying that the cocrystal should show balanced, e.g., ambipolar, charge transport.

To investigate the conduction mechanism in CESA grown PTZ−TCNQ cocrystal OFETs, transfer curves were measured at temperatures between 120 and 350 K and the results used to determine the off-current and field-effect mobility. Transfer curves at various temperatures are shown in Figure 12. With increasing temperature, the curves displayed a significant

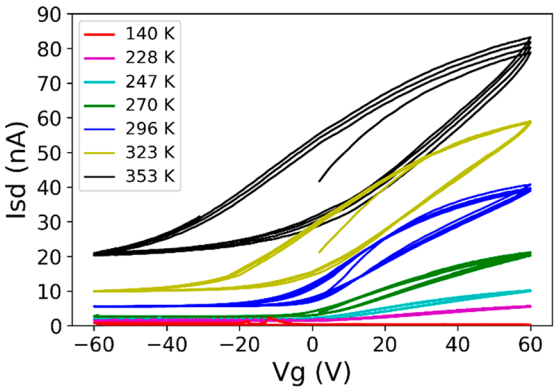

Figure 12. Transfer curves at various device temperatures.

increase in off-current compared to the device's room temperature performance. The off-current increased from 5 to 21 nA as the temperature increased from 296 to 353 K. However, the overall slope of the linear portion of the response curve, and thus the device's calculated field effect mobility, only changed slightly in this range. Upon cooling, the transfer curves showed a similar trend, as shown in the figure. The off-current decreases with temperature and trends toward a value of zero for the lowest temperatures. In addition, the slope of the response curve also decreases with temperature, suggesting that charge carrier mobility decreased as electrons became unable to escape from localized states.

The calculated field effect mobility versus temperature is shown in Figure 13. The mobility values were calculated from

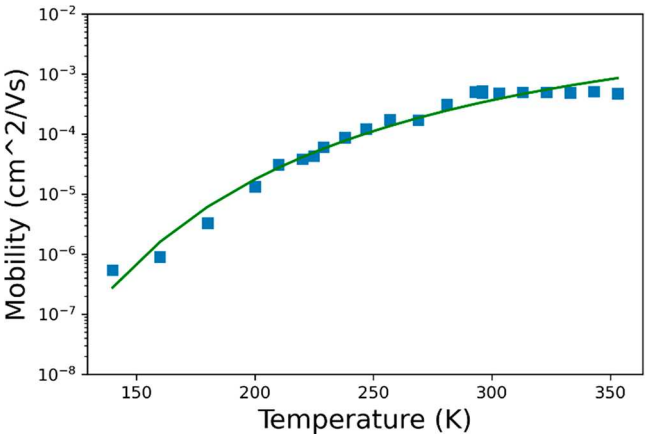

Figure 13. Electron mobility vs temperature data and least-squares fit to eq 5.

the slope of the forward sweep of the transfer curves shown in Figure 12 using eq 4. This behavior of mobility vs temperature is indicative of a hopping mode of charge transport, as compared to band-like transport in which the primary impedance to conduction is lattice scattering, leading to lower mobility as temperature is increased.[53]

Injected charge in weak CT cocrystals such as PTZ−TCNQ will be localized on electron acceptors. This will be accompanied by some rearrangement of the local charge as well as changes in both intra- and intermolecular bond lengths, i.e., formation of polarons. This has been observed in numerous single-component molecular crystals. Transport of this charge to the next acceptor will require thermal fluctuations to overcome the energy barrier of the order of

https://doi.org/10.1021/acsaelm.2c01160
ACS Appl. Electron. Mater. XXXX, XXX, XXX−XXX

the reorganization energy E_A, leading to the following dependence of mobility on temperature:[57]

$$\mu \propto T^{-3/2} e^{-E_A/k_B T} \quad (5)$$

Shuai et al. found a similar scaling for the mobility in triphenylamine dimers using Marcus transport theory to model the charge transport as a Brownian process.[58]

The scaling of this equation predicts that the charge carrier mobility should decrease at low temperatures, with the exponential hopping term dominating. However, at high temperatures phonon scattering dominates, giving a power law dependence of the mobility. A least-squares fit of eq 5 to the data in Figure 13 gave a value of E_A = 190 meV. This is close to the value of 217 meV that was calculated by Geng et al. using the superexchange model described earlier.[28]

Nonzero off-currents are typically attributed to impurities in the material. As temperature increases, more of these impurity charge carriers may be thermally activated, also leading to an Arrhenius-type temperature dependence (see Figure S7).

CONCLUSIONS

The CESA method was used to create oriented ribbons of the charge transfer cocrystal PTZ−TCNQ which were incorporated into an organic FET. Transfer curves of the devices showed primarily electron transport. Although this is contrary to predictions of low effective mass for both holes and electrons, the details of the device such as electrode work function and presence of traps can affect measured mobilities, and so these results do not necessarily imply that this material is purely an n-type semiconductor. Maximum mobilities of the order of 10^{-4}−10^{-3} $cm^2/(V\ s)$ were found, similar to values reported for other similar molecular crystals[58] but not as large as the 1.7 and 0.4 $cm^2/(V\ s)$ reported for PTZ and TCNQ as individual crystals at room temperature.[53] Temperature-dependent measurements of the mobility displayed characteristics of hopping transport.

ASSOCIATED CONTENT

Supporting Information

The Supporting Information is available free of charge at https://pubs.acs.org/doi/10.1021/acsaelm.2c01160.

Details of the deposition of metal electrodes for FET fabrication (Figure S1), PXRD spectra at different orientations (Figure S2), temperature-dependent Raman measurement of PTZ−TCNQ microribbons (Figures S3−S5), Kelvin probe force microscopy measurements (Figure S6), and temperature dependence of the off-current of PTZ−TCNQ FETs (Figure S7) (PDF)

AUTHOR INFORMATION

Corresponding Author

Edward Van Keuren − *Department of Physics and Institute for Soft Matter Synthesis and Metrology, Georgetown University, Washington, D.C. 20057, United States;* orcid.org/0000-0001-8348-7587; Email: erv@georgetown.edu

Authors

Scott Melis − *Department of Physics and Institute for Soft Matter Synthesis and Metrology, Georgetown University, Washington, D.C. 20057, United States;* orcid.org/0000-0001-8512-1589

Samantha Hung − *Department of Physics and Institute for Soft Matter Synthesis and Metrology, Georgetown University, Washington, D.C. 20057, United States;* orcid.org/0000-0001-9448-0962

Chaitali Bagade − *Department of Physics and Institute for Soft Matter Synthesis and Metrology, Georgetown University, Washington, D.C. 20057, United States*

Yuri Chung − *Department of Physics and Institute for Soft Matter Synthesis and Metrology, Georgetown University, Washington, D.C. 20057, United States*

Eleni Hughes − *Department of Physics and Institute for Soft Matter Synthesis and Metrology, Georgetown University, Washington, D.C. 20057, United States;* orcid.org/0000-0002-4436-2615

Xinran Zhang − *Department of Physics and Institute for Soft Matter Synthesis and Metrology, Georgetown University, Washington, D.C. 20057, United States*

Paola Barbara − *Department of Physics and Institute for Soft Matter Synthesis and Metrology, Georgetown University, Washington, D.C. 20057, United States*

Peize Han − *Department of Physics and Institute for Soft Matter Synthesis and Metrology, Georgetown University, Washington, D.C. 20057, United States*

Tingting Li − *Department of Physics and Institute for Soft Matter Synthesis and Metrology, Georgetown University, Washington, D.C. 20057, United States*

Daniel McCusker − *Department of Physics and Institute for Soft Matter Synthesis and Metrology, Georgetown University, Washington, D.C. 20057, United States*

Robert Hartsmith − *Department of Physics and Institute for Soft Matter Synthesis and Metrology, Georgetown University, Washington, D.C. 20057, United States*

Jeffery Bertke − *Department of Chemistry, Georgetown University, Washington, D.C. 20057, United States;* orcid.org/0000-0002-3419-5163

Pratibha Dev − *Department of Physics and Astronomy, Howard University, Washington, D.C. 20059, United States*

Iris Stone − *Department of Physics, George Mason University, Fairfax, Virginia 22030, United States; Quantum Science and Engineering Center, George Mason University, Fairfax, Virginia 22030, United States*

Jaydeep Joshi − *Department of Physics, George Mason University, Fairfax, Virginia 22030, United States; Quantum Science and Engineering Center, George Mason University, Fairfax, Virginia 22030, United States;* orcid.org/0000-0002-8024-0586

Patrick Vora − *Department of Physics, George Mason University, Fairfax, Virginia 22030, United States; Quantum Science and Engineering Center, George Mason University, Fairfax, Virginia 22030, United States;* orcid.org/0000-0003-3967-8137

Complete contact information is available at: https://pubs.acs.org/10.1021/acsaelm.2c01160

Notes

The authors declare no competing financial interest.

ACKNOWLEDGMENTS

The authors gratefully acknowledge support from the National Science Foundation MRI Program for acquisition of the

Raman instrument used in these studies (NSF CHE-1429079), the Research Experience for Undergraduates program (DMR-1358978) for support of R.H. and S.H., and Grant NSF-2132098 for general support of the project. S.M. thanks the Walter G. Mayer Endowed Scholarship Fund for support. P.D. was supported by NSF Grant OAC-2118099. P.D. acknowledges the computational support by the Extreme Science and Engineering Discovery Environment (XSEDE) under Project PHY180014, which is supported by NSF Grant ACI-1548562. Y.C. was supported by the NASA DC Space Grant.

REFERENCES

(1) Tsumura, A.; Koezuka, H.; Ando, T. Macromolecular Electronic Device: Field-Effect Transistor with a Polythiophene Thin Film. *Appl. Phys. Lett.* **1986**, *49*, 1210−1212.
(2) Horowitz, G. Organic Field-Effect Transistors. *Adv. Mater.* **1998**, *10*, 365−377.
(3) Zaumseil, J.; Sirringhaus, H. Electron and Ambipolar Transport in Organic Field-Effect Transistors. *Chem. Rev.* **2007**, *107*, 1296−1323.
(4) Meijer, E. J.; de Leeuw, D. M.; Setayesh, S.; van Veenendaal, E.; Huisman, B. -H.; Blom, P. W. M.; Hummelen, J. C.; Scherf, U.; Klapwijk, T. M. Solution-Processed Ambipolar Organic Field-Effect Transistors and Inverters. *Nat. Mater.* **2003**, *2*, 678−682.
(5) Wang, W.; Luo, L.; Sheng, P.; Zhang, J.; Zhang, Q. Multifunctional Features of Organic Charge-Transfer Complexes: Advances and Perspectives. *Chem.—Eur. J.* **2021**, *27*, 464−490.
(6) Huang, Y.; Wang, Z.; Chen, Z.; Zhang, Q. Organic Cocrystals: Beyond Electrical Conductivities and Field-Effect Transistors (FETs). *Angew. Chem.* **2019**, *131*, 9798−9813.
(7) Goetz, K. P.; Vermeulen, D.; Payne, M. E.; Kloc, C.; McNeil, L. E.; Jurchescu, O. D. Charge-Transfer Complexes: New Perspectives on an Old Class of Compounds. *J. Mater. Chem. C* **2014**, *2*, 3065−3076.
(8) Tayi, A. S.; Kaeser, A.; Matsumoto, M.; Aidi, T.; Stupp, S.; et al. Room-Temperature Ferroelectricity in Supramolecular Networks of Charge-Transfer Complexes. *Nat. Chem.* **2012**, *488*, 485−489.
(9) Jerome, D.; Mazaud, A.; Ribault, M.; Bechgaard, K. Superconductivity in a Synthetic Organic Conductor $(TMTSF)_2PF_6$. *J. Phys., Lett.* **1980**, *41*, L95−L98.
(10) Schaffert, R. M.; Schaffert, R. M. A New High-Sensitivity Organic Photoconductor for Electrophotography. *IBM J. Res. Dev* **1971**, *15*, 75−89.
(11) Su, B.; Wu, Y.; Jiang, L. The Art of Aligning One-Dimensional (1D) Nanostructures. *Chem. Soc. Rev.* **2012**, *41*, 7832−7856.
(12) McGlynn, S. P. Energetics of Molecular Complexes. *Chem. Rev.* **1958**, *58*, 1113−1157.
(13) Takahashi, Y.; Hasegawa, T.; Abe, Y.; Tokura, Y.; Nishimura, K.; Saito, G. Tuning of Electron Injections for N-Type Organic Transistor Based on Charge-Transfer Compounds. *Appl. Phys. Lett.* **2005**, *86*, 063504.
(14) Zhu, L.; Yi, Y.; Fonari, A.; Corbin, N. S.; Coropceanu, V.; Bredas, J. Electronic Properties of Mixed-Stack Organic Charge-Transfer Crystals. *J. Phys. Chem. C* **2014**, *118*, 14150−14156.
(15) Bisri, S. Z.; Piliego, C.; Gao, J.; Loi, M. A. Outlook and Emerging Semiconducting Materials for Ambipolar Transistors. *Adv. Mater.* **2014**, *26*, 1176−1199.
(16) Mitchell, S. C. Phenothiazine: The Parent Molecule. *Curr. Drug Targets* **2006**, *7*, 1181−1189.
(17) Bright, A.; Garito, A.; Heeger, A. Optical Conductivity Studies in a One-Dimensional Organic Metal: Tetrathiofulvalene Tetracyanoquinodimethan (TTF) (TCNQ). *Phys. Rev. B: Condens. Matter Mater. Phys.* **1974**, *10*, 1328−1342.
(18) Vincent, V. M.; Wright, J. D. Photoconductivity and Crystal Structure of Organic Molecular Complexes. *J. Chem. Soc., Faraday Trans. 1* **1974**, *70*, 58−71.
(19) Bhat, S. N. Electron Donating Properties of Phenothiazine and Methylphenothiazine. *Indian J. Chem., Sect. A: Inorg., Phys., Theor. Anal* **1976**, *14*, 791−792.
(20) Tanaka, J.; Tanaka, M. Reflection Spectra of the Crystalline Electron Donor-Acceptor Complexes of TCNQ. *Mol. Cryst. Liq. Cryst.* **1979**, *52*, 525−529.
(21) Li, J.; Zhang, S.; Wang, F.; Wu, H.; Shi, L.; Pan, G. Facile Fabrication of Phenothiazine-Tetracyanoquinodimethane Co-Crystal Microwires with Ambipolar Charge Transport Characteristics. *Mater. Lett.* **2018**, *210*, 161−164.
(22) Diao, Y.; Shaw, L.; Bao, Z.; Mannsfeld, S. C. B. Morphology Control Strategies for Solution-Processed Organic Semiconductor Thin Films. *Energy Environ. Sci.* **2014**, *7*, 2145−2159.
(23) Karthaus, O.; Nagata, S.; Kiyono, Y.; Ito, S.; Miyasaka, H. Control of Crystal Morphology of a Fluorescent Charge Transfer Complex by Dewetting on a Mica Surface. *Colloids Surf., A* **2008**, *313−314*, 571−575.
(24) Jang, J.; Nam, S.; Im, K.; Hur, J.; Cha, S. N.; Kim, J. J. M.; Son, H. B.; Suh, H.; Loth, M. A.; Anthony, J. E.; Park, J.; Park, C. E.; Kim, J. J. M.; Kim, K. Highly Crystalline Soluble Acene Crystal Arrays for Organic Transistors: Mechanism of Crystal Growth during Dip-Coating. *Adv. Funct. Mater.* **2012**, *22*, 1005−1014.
(25) Zhao, H.; Wang, Z.; Dong, G.; Duan, L. Fabrication of Highly Oriented Large-Scale TIPS Pentacene Crystals and Transistors by the Marangoni Effect-Controlled Growth Method. *Phys. Chem. Chem. Phys.* **2015**, *17*, 6274−6279.
(26) Han, W.; Lin, Z. Learning from "Coffee Rings": Ordered Structures Enabled by Controlled Evaporative Self-Assembly. *Angew. Chem., Int. Ed* **2012**, *51*, 1534−1546.
(27) Bi, S.; He, Z.; Chen, J.; Li, D. Solution-Grown Small-Molecule Organic Semiconductor with Enhanced Crystal Alignment and Areal Coverage for Organic Thin Film Transistors. *AIP Adv.* **2015**, *5*, 077170.
(28) Geng, H.; Zheng, X.; Shuai, Z.; Zhu, L.; Yi, Y. Understanding the Charge Transport and Polarities in Organic Donor-Acceptor Mixed-Stack Crystals: Molecular Insights from the Super-Exchange Couplings. *Adv. Mater.* **2015**, *27*, 1443−1449.
(29) Van Keuren, E.; Pornrungroj, C.; Fu, C.; Zhang, X.; Okada, S.; Katsuyama, H.; Kikuchi, K.; Onodera, T.; Oikawa, H. Polydiacetylene Ribbons Formed using the Controlled Evaporative Self-Assembly (CESA) Method. *MRS Commun.* **2019**, *9*, 229−235.
(30) Van Keuren, E.; Melis, S.Charge Transfer Nanocrystals for Optical and Electronic Applications. In *Nanocomposites for Photonic and Electronic Applications*; Kassab, L. R. P., Ribiero, S. J. L., Rangel-Rojo, R., Eds.; Elsevier: 2020; pp 139−165.
(31) Kobayashi, H. Sinusoidal Structure of the 1:1 Complex of Phenothiazine and 7,7,8,8-Tetracyanoquinodimethane, PTZ-TCNQ. *Acta Crystallogr., Sect. B: Struct. Crystallogr. Cryst. Chem.* **1974**, *30*, 1010−1017.
(32) McDowell, J. The crystal and molecular structure of phenothiazine. *Acta Crystallogr., Sect. B: Struct. Crystallogr. Cryst. Chem.* **1976**, *32*, 5−10.
(33) Salzillo, T.; Masino, M.; Kociok-Köhn, G.; Di Nuzzo, D.; Venuti, E.; Della Valle, R. G.; Vanossi, D.; Fontanesi, C.; Girlando, A.; Brillante, A.; Da Como, E. Structure, Stoichiometry, and Charge Transfer in Cocrystals of Perylene with TCNQ-F_x. *Cryst. Growth Des* **2016**, *16*, 3028−3036.
(34) Girlando, A.; Pecile, C. Polarized Raman Spectra of TCNQ and TCNQ-D4 Single Crystals. *Spectrochim. Acta, Part A* **1973**, *29*, 1859−1878.
(35) Kure, B.; Morris, M. Raman Spectra of Phenothiazine and Some Pharmaceutical Derivatives. *Talanta* **1976**, *23*, 398−400.
(36) Matsuzaki, S.; Kuwata, R.; Toyoda, K. Raman-Spectra of Conducting Tcnq Salts - Estimation of the Degree of Charge-Transfer from Vibrational Frequencies. *Solid State Commun.* **1980**, *33*, 403−405.
(37) Van Keuren, E.; Nishida, M. Synthesis of Nanocomposite Materials using the Reprecipitation Method. *Comput. Mater. Con* **2010**, *409*, 61−77.

https://doi.org/10.1021/acsaelm.2c01160
ACS Appl. Electron. Mater. XXXX, XXX, XXX−XXX

(38) Kozawa, K.; Hoshizaki, T.; Uchida, T. Classification of Phenothiazine Complexes by Structure and Electronic Properties. *Bull. Chem. Soc. Jpn.* **1991**, *64*, 2039−2044.
(39) Frisch, M. J.; Trucks, G. W.; Schlegel, H. B.; Scuseria, G. E.; Robb, M. A.; Cheeseman, J. R.; Scalmani, G.; Barone, V.; Petersson, G. A.; Nakatsuji, H.; Li, X.; Caricato, M.; Marenich, A.; Bloino, J.; Janesko, B. G.; Gomperts, R.; Mennucci, B.; Hratchian, H. P.; Ortiz, J. V.; Izmaylov, A. F.; Sonnenberg, J. L.; Williams-Young, D.; Ding, F.; Lipparini, F.; Egidi, F.; Goings, J.; Peng, B.; Petrone, A.; Henderson, T.; Ranasinghe, D.; Zakrzewski, V. G.; Gao, J.; Rega, N.; Zheng, G.; Liang, W.; Hada, M.; Ehara, M.; Toyota, K.; Fukuda, R.; Hasegawa, J.; Ishida, M.; Nakajima, T.; Honda, Y.; Kitao, O.; Nakai, H.; Vreven, T.; Throssell, K.; Montgomery, Jr., J. A.; Peralta, J. E.; Ogliaro, F.; Bearpark, M.; Heyd, J. J.; Brothers, E.; Kudin, K. N.; Staroverov, V. N.; Keith, T.; Kobayashi, R.; Normand, J.; Raghavachari, K.; Rendell, A.; Burant, J. C.; Iyengar, S. S.; Tomasi, J.; Cossi, M.; Millam, J. M.; Klene, M.; Adamo, C.; Cammi, R.; Ochterski, J. W.; Martin, R. L.; Morokuma, K.; Farkas, O.; Foresman, J. B.; Fox, D. J.*Gaussian 09*, Revision C.01; Gaussian, Inc.: Wallingford, CT, 2016.
(40) Becke, A. D. Density-Functional Thermochemistry. III. the Role of Exact Exchange. *J. Chem. Phys.* **1993**, *98*, 5648.
(41) Lee, C.; Yang, W.; Parr, R. G. Development of the Colle-Salvetti Correlation-Energy Formula into a Functional of the Electron Density. *Phys. Rev. B* **1988**, *37*, 785−789.
(42) Stephens, P. J.; Devlin, F. J.; Ashvar, C. S.; Chabalowski, C. F.; Frisch, M. J. Theoretical Calculation of Vibrational Circular Dichroism Spectra. *Faraday Discuss.* **1994**, *99*, 103.
(43) Dev, P.; Agrawal, S.; English, N. J. Determining the Appropriate Exchange-Correlation Functional for Time-Dependent Density Functional Theory Studies of Charge-Transfer Excitations in Organic Dyes. *J. Chem. Phys.* **2012**, *136*, 224301.
(44) Yoshida, H.; Ehara, A.; Matsuura, H. Density Functional Vibrational Analysis using Wavenumber-Linear Scale Factors. *Chem. Phys. Lett.* **2000**, *325*, 477−483.
(45) NIST Computational Chemistry Comparison and Benchmark Database NIST Standard Reference Database Number 101, 2020.
(46) Torrance, J. B.; Vazquez, J. E.; Mayerle, J. J.; Lee, V. Y. Discovery of a Neutral-to-Ionic Phase Transition in Organic Materials. *Phys. Rev. Lett.* **1981**, *46*, 253−257.
(47) Bloor, J. E.; Gilson, B. R.; Haas, R. J.; Zirkle, C. L. Electron-Donating Properties of Phenothiazine and Related Compounds. *J. Med. Chem.* **1970**, *13*, 922−925.
(48) Zhu, G.; Wang, L. Communication: Vibrationally Resolved Photoelectron Spectroscopy of the Tetracyanoquinodimethane (TCNQ) Anion and Accurate Determination of the Electron Affinity of TCNQ. *J. Chem. Phys.* **2015**, *143*, 221102.
(49) Newman, C. R.; Frisbie, C. D.; Da Silva Filho, D. A.; Brédas, J. L.; Ewbank, P. C.; Mann, K. R. Introduction to Organic Thin Film Transistors and Design of N-Channel Organic Semiconductors. *Chem. Mater.* **2004**, *16*, 4436−4451.
(50) Mayer, T.; Hein, C.; Mankel, E.; Jaegermann, W.; Muller, M. M.; Kleebe, H.-J. Fermi level positioning in organic semiconductor phase mixed composites: The internal interface charge transfer doping model. *Org. Electron* **2012**, *13*, 1356−1364.
(51) Egginger, M.; Bauer, S.; Schwödiauer, R.; Neugebauer, H.; Sariciftci, N. S. Current Versus Gate Voltage Hysteresis in Organic Field Effect Transistors. *Monatsh. Chem.* **2009**, *140*, 735−750.
(52) Sze, S. M.; Ng, K. K. In *Physics of Semiconductor Devices*; Wiley-Interscience: Hoboken, NJ, 2007.
(53) Pope, M.; Swenberg, C. In *Electronic Processes in Organic Crystals and Polymers*; Oxford Science Publications: Oxford, 1999; pp 337−369.
(54) Mott, N. F.; Davis, E. A. In *Electronic Processes in Non-crystalline Materials*; Oxford University Press: Oxford, 2012.
(55) Vora, P. M.; Gopu, P.; Rosario-Canales, M.; Perez, C. R.; Gogotsi, Y.; Santiago-Aviles, J. J.; Kikkawa, J. M. Correlating Magnetotransport and Diamagnetism of Sp{2}-Bonded Carbon Networks through the Metal-Insulator Transition. *Phys. Rev. B* **2011**, *84*, 155114.
(56) Geng, H.; Zhu, L.; Yi, Y.; Zhu, D.; Shuai, Z. Superexchange Induced Charge Transport in Organic Donor−Acceptor Cocrystals and Copolymers: A Theoretical Perspective. *Chem. Mater.* **2019**, *31*, 6424−6434.
(57) Coropceanu, V.; Cornil, J.; da Silva Filho, D.; Olivier, Y.; Silbey, R.; Bredas, J. Charge Transport in Organic Semiconductors. *Chem. Rev.* **2007**, *107*, 926−952.
(58) Shuai, Z.; Wang, L.; Song, C. In *Theory of Charge Transport in Carbon Electronic Materials*; Springer: Heidelberg, 2012; pp 7−41.

https://doi.org/10.1021/acsaelm.2c01160
ACS Appl. Electron. Mater. XXXX, XXX, XXX−XXX